Variation of adsorption effects in coals with different particle sizes induced by differences in microscopic adhesion

Qifeng Jia [a,b,c], Dameng Liu [a,b,*], Yidong Cai [a,b], Yanbin Yao [a,b], Yuejian Lu [a,b], Yingfang Zhou [c,d]

[a] *School of Energy Resources, China University of Geosciences, Beijing 100083, China*

[b] *Coal Reservoir Laboratory of National Engineering Research Center of CBM Development & Utilization, China*

University of Geosciences, Beijing 100083, China

[c] *School of Engineering, Fraser Noble Building, King's College, University of Aberdeen, AB24 3UE Aberdeen, UK*

[d] *Department of Energy Resources, University of Stavanger, Stavanger, 4021, Norway*

* Corresponding author at: School of Energy Resources, China University of Geosciences, Beijing 100083, China.

E-mail address: dmliu@cugb.edu.cn (D. Liu), Tel: +86-10-82323971; fax: + 86-10-82326850.

Abstract

The swelling strain caused by methane adsorption in coal affects reservoir permeability, further complicating the propagation of fluid pressure. The impact of different scales of pores in coal on the adsorption behavior was investigated by combining the reaction heat apparatus C80 and atomic force microscopy (AFM), followed by characterization of adsorption effect variation in coals with different particle sizes due to adhesion differences. The results show that the absolute adsorption volume (AAV) of the high-rank coal sample Chengzhuang (CZ) of 0.85-2.00 mm is 1.06 times higher than that of the medium-rank coal sample Qiyi (QY) under the pressure of 4.2 MPa. With the increase of pressure, more desorption occurs at different sites of adsorbed phase,

1

21 resulting in the increase in the density of the free phase methane increasing the gap

22 between AAV and excess adsorption volume (EAV). The larger the particle size of coal,

23 the smaller the temperature variation during adsorption. In the AFM measurements, CZ

24 containing 2026 adsoption pores exhibits stronger heterogeneity than QY, leading to

25 the formation of more capillary condensation of methane. For the adsorption heat,

26 methane tends to occupy sites with high adsorption potential at the beginning of

27 adsorption to release large amounts of heat. Moreover, the adhesion force distribution

28 of QY is more uniform than that of CZ, mainly concentrated between 1.5 and 3.0 nN.

29 Subject to microscopic adhesion force, methane molecules in the effective adhesion

30 region can be stably adsorbed to pores. Temperature affects the heterogeneity of

31 adhesion, mainly the higher the temperature, the more concentrated the distribution of

32 adhesion in coal. The findings contribute to the clarification of the adsorption kinetics

33 of nanoscale carriers in coal reservoirs.

34 *Keywords:* Adsorption heat; Desorption; Temperature; Microscopic adhesion;

35 Condensation

1. Introduction

37 The efficient exploitation of coalbed methane (CBM), as a key component of

38 unconventional natural gas, is of great strategic importance for the early realization of

39 carbon neutrality [1-4]. Coal is a porous medium with a large internal specific surface

40 area that thus exhibits adsorption effects on gases [5, 6]. Adsorption of coal involves a

41 process of microporous filling or multilayer adsorption, rather than simple monolayer

adsorption [7]. In general, the deformation of the adsorption expansion of coal exceeds that of the desorption contraction, making the energy change of the adsorption process not exactly the same as that of the desorption process [8-10]. With the increase in deformation degree, the aromatization and ring condensation of coal are significantly enhanced [11, 12], resulting in the gradual increase of Langmuir volume. Compared with primary structure coal, the adsorption capacity of mylonite coal is stronger.

The adsorption effect of coal is influenced by coal quality, physicochemical structure, temperature, pressure and stress [13-15]. Zhang et al. [16] found that the desorption rate of anthracite after plasma treatment was greater than that of bituminous coal by combining electric pulse fracturing with isothermal adsorption tests. A large amount of heat carried by plasma increases the temperature, leading to a decrease in the adsorption capacity of coal [17]. Liu et al. [18] believed that the adsorption process changed from the collision phase between pore surface and gas molecules to the intermediate phases of single-molecule adsorption and multilayer adsorption with increasing relative pressure. Due to the extensive development of micropores, most of the isothermal curves of adsorption and desorption in coal show a significant hysteresis [19]. Gou et al. [20] tested the structural characteristics of pore-fracture at different scales using field emission scanning electron microscope (FE-SEM) and computerized tomography (CT), concluding that micropores and mesopores provided large adsorption space for adsorbed gases. Chen et al. [21] showed that the internal structure of coal was changed after methane adsorption by low-temperature liquid nitrogen adsorption tests, resulting in higher electrical conductivity. Additionally, moisture

64 altered the wettability of coal [22], leading to enhanced electrical conductivity. The

65 difference in wettability of different components in coal makes the process of methane

66 adsorption more complicated [23]. Fu et al. [24] revealed that microwave radiation

67 reduced the adsorption pores with pore size below 10 nm and increased the total content

68 of C-O and COOH. In particular, microwave radiation can change the chemical

69 properties of coal, causing a decrease in the affinity of coal for methane adsorption [25].

70 According to the characteristics of adsorption-induced swelling, Zhang et al. [26]

71 suggested that the apparent volume expansion decreased with increasing strain at the

72 same adsorption pressure. Under the same temperature and pressure conditions, the

73 factors affecting the adsorption expansion of coal bodies include adsorbent molecules,

74 chemical potential and stress conditions [27, 28]. In the process of methane adsorption,

75 the gas molecules start to be stored in the macromolecular structure network of coal as

76 adsorbed state [29]. After reaching the peak strain, the shrinkage effect occurs in the

77 coal matrix [18].

78   Subject to multi-phase tectonic stress, the number of micropores in tectonic coals

79 gradually increases in the same metamorphic environment [30]. For the thermal effect

80 of adsorption, the impact of porous structure is more significant than that of gas

81 injection [31, 32]. The adsorption heat is the conversion energy between adsorbed gas

82 and free gas [7], which can be used to predict the adsorption isotherms at different

83 temperatures and pressures. Moreover, the adsorption heat can characterize the

84 temperature evolution of coal, the energy distribution of sites and the heterogeneity of

85 surface energy [13, 23].

86 In the past few years, many scholars have extensively studied the adsorption

87 capacity, electrical characteristics, multilayer adsorption mechanisms, wettability

88 differences and adsorption-deformation effects of coals with different metamorphic

89 degrees [7, 14, 33, 34]. Interestingly, the thermal expansion effect of methane adsorbed

90 by medium-high rank coals during fracturing was quantified [18, 35]. However, few

91 studies have been reported to reveal the adsorption mechanism of coal from the

92 perspective of microscopic adhesion considering the combined effects of van der Waals,

93 capillary and Coulomb forces. In particular, we have not seen existing studies that have

94 explored the effect of adhesion on adsorption effects at different temperatures in coal.

95 Besides, there is little research on the accurate assessment of nanoscale pores on the

96 adsorption heat variation of coals with different particle sizes. These aspects of the

97 research essentially address the difficulty of improving the desorption of coal reservoirs

98 through chemical fracturing fluids.

99 In this work, we have investigated the changes in the adsorption behavior of coals

100 with different particle sizes caused by adhesion differences using the combination of

101 reaction heat apparatus C80 and atomic force microscopy (AFM). This was

102 accomplished by first analyzing the adsorption properties of coals with different particle

103 sizes and then revealing the constraint mechanism of temperature on the adsorption

104 behavior. Subsequently, the influence of different scales of pores in coal on the

105 adsorption effect was quantified, followed by a realistic assessment of the adsorption

106 heat variation of coals with different particle sizes at different temperature conditions.

107 To further clarify the mechanism of methane adsorption by coal, the adsorption effect

108   of coals with different particle sizes was analyzed from the perspective of microscopic

109   adhesion considering the combined effect of van der Waals, capillary and Coulomb

110   forces. Thus, this study contributes to clarifying the differences in production

111   enhancement of CBM wells in different types of reservoirs after reaching the critical

112   desorption pressure.

2. Sample and experimental systems

113

2.1. Sample and preparation

114

115   Coal samples (Fig. 1), collected from Chengzhuang (CZ) and Qiyi (QY) coal mines

116   in the Qinshui Basin, were used to test the basic coal petrology parameters. The

117   maximum vitrinite reflectance ($R_{o,\ max}$) was determined by a Leitz MPV-III

118   microphotometer and the industrial components were evaluated by a fully automated

119   industrial analyzer, following international standards of ISO 7404.3–1994 and ISO

120   7404.5–1994 [18, 35, 36]. As indicated in Table 1, the $R_{o,\ max}$ of CZ is greater than that

121   of QY, while the volatile matter is smaller than that of QY. This demonstrates that CZ

122   is more deeply intruded by magma, resulting in a greater degree of coalification [37,

123   38]. CZ exhibits the $R_{o,\ max}$ of 2.98, corresponding to high-rank coal, while QY with the

124    $R_{o,\ max}$ of 1.72 belongs to medium-rank coal. After that, the different coal samples were

125   crushed, followed by the extraction of coal powder of 0.85-2.00 mm, 0.43-0.85 mm and

126   0.18-0.25 mm through the screen sieve, respectively. To ensure the accuracy of the

127   adsorption experiments, methane with a concentration of 99.99% was used to complete

128   the adsorption kinetics test of this study.
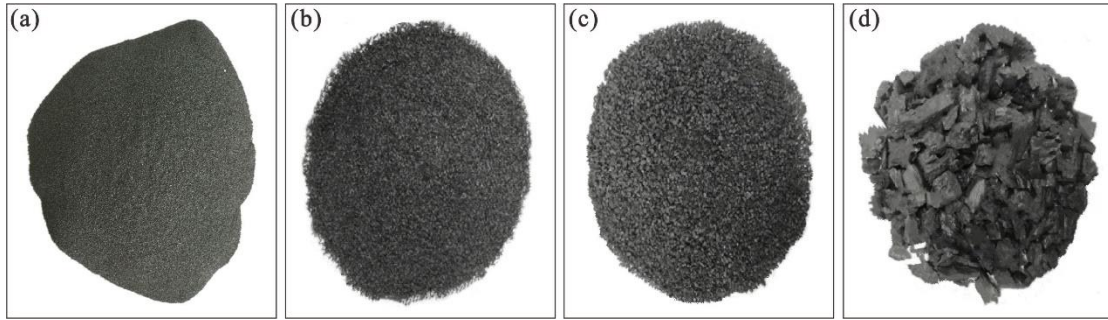
Fig. 1. Experimental coal samples at different scales. (a) 0.18-0.25 mm; (b) 0.43-0.85 mm; (c) 0.85-2.00 mm; (d) 10-15 mm.

Table 1 Basic information of the experimental coal sample.

Samples	Depth (m)	$R_{o, max}$ (%)	Per (mD)	Proximate analysis (%)				Coal maceral composition (%)	
				M_{ad}	A_{ad}	V_{ad}	FC_{ad}	V	I
CZ	521	2.98	0.04	0.61	18.16	6.52	74.71	90.3	9.7
QY	483	1.72	0.07	1.36	9.79	13.69	75.16	92.7	7.3

Note: Per, permeability; M_{ad}, moisture (air-dried basis); A_{ad}, ash (dry basis); V_{ad}, volatile matter (dry, ash-free basis); FC_{ad}, Fixed carbon (air-dried basis); V, vitrinite; I, inertinite; E, exinite.

2.2. Testing Instruments

The experimental system for this study consists of reaction heat apparatus C80 and AFM. The model C80 reaction heat apparatus (Fig. 2a), from the State Key Laboratory Cultivation base for Gas Geology and Control of Henan Polytechnic University in the Province and Ministry, is equipped with a reaction kettle, heating program, signal converter, sample cylinder and reference cylinder. The entire instrument runs at a maximum temperature of 300 °C with a maximum ramp rate of 2 K/min. The seal ring of the reaction kettle is composed of tetrafluoroethylene at a maximum operating temperature of 220 °C. If the temperature of the reaction kettle exceeds 220 °C during the experiment, the seal ring needs to be removed, which results in a larger error in the

145 measured adsorption heat [39]. Hence, the heating process of coal samples should not

146 be higher than the limited temperature of the seal ring as much as possible [40]. To

147 allow for sufficient pressure redundancy, basic pressure changes need to be estimated

148 before the high-pressure treatment of the sample cylinder, especially for samples that

149 give off large amounts of gas [23]. Since the sample cylinder is prone to rupture or

150 deformation due to overpressure, this can lead to damage to the reaction heat instrument

151 [41]. Therefore, the pressure of the sample cylinder should not exceed 20 MPa during

152 the whole experiment.
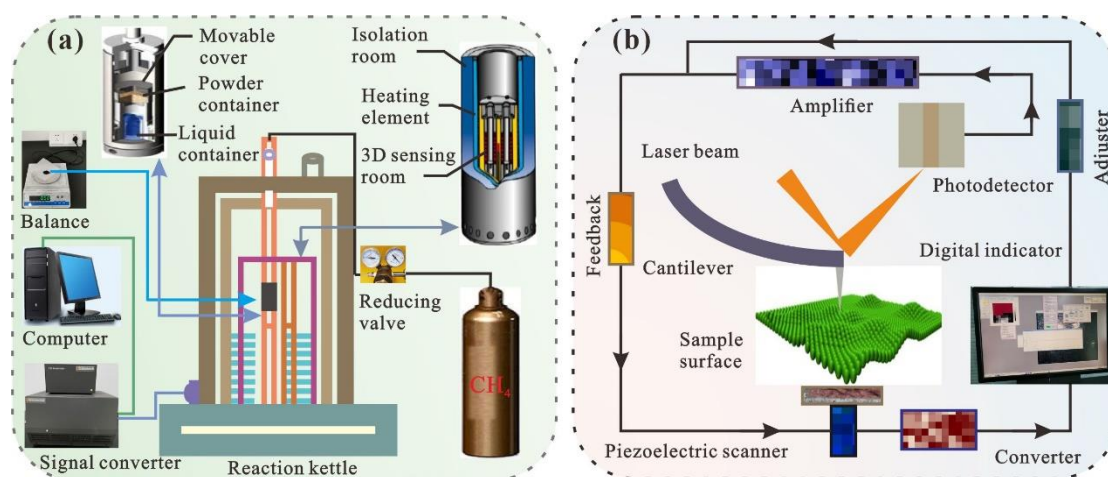
Fig. 2. Schematic diagram of the principle of the experimental setup. (a) Reaction heat

apparatus C80; (b) AFM.

156 AFM (Fig. 2b), model Dimension, was used to measure the roughness and adhesion

157 properties of coal. In the contact mode, the height undulation of the sample surface can

158 be measured [22]. In another PeakForce QNM^{TM} mode, the mechanical modulus,

159 adhesion, deformation and other physical properties of the sample can be obtained

160 while imaging at high resolution [42]. The entire device adopts Digital Q control

161 technology, which allows digital control of the Q value to improve the signal-to-noise

162   ratio. Additionally, the AFM includes an anti-vibration device to prevent the occurrence

163   of low-frequency resonance. This instrument has a scanning range of $90 \times 90 \times 10$ μm

164   in the X, Y and Z directions, with a thermal drift level of less than 0.2 nm/min. The

165   vertical and horizontal resolutions exhibit 0.01 nm and 0.1 nm, respectively.

166   *2.3. Experimental procedures*

167   The whole experimental procedure is divided into four steps: sample processing,

168   adsorption test, adsorption heat measurement and AFM scan. In the process of sample

169   processing, 60 g coal samples of different scales were dried and then put into the

170   adsorption tank respectively for experiments. To maintain a constant temperature, the

171   test cell was in an oil bath consisting of a stainless steel reference tank and a sample

172   tank. According to the field reservoir conditions, adsorption experiments were

173   conducted under different temperatures (25 °C, 30 °C, 35 °C, 40 °C, 45 °C and 50 °C)

174   at a maximum pressure of 8 MPa. The whole adsorption test system consists of gas

175   cylinder, pressure sensor, signal receiver, thermostat, sample and reference cylinders.

176   The isothermal adsorption experiments were carried out with 99.99% methane gas at

177   different temperatures. According to the standard GB/T19560-2008 [18], the adsorption

178   volume was determined experimentally by static capacity. The volume of methane gas

179   adsorbed at equilibrium at the same temperature and under different pressure conditions

180   was measured immediately after placing the measured coal sample with balanced water

181   content in a sealed container. Subsequently, the Langmuir volume (V_L), pressure (P_L)

182   and isothermal adsorption curves were calculated based on the Langmuir monolayer

183   adsorption theory. For adsorption heat testing, we should make sure that the O-ring and

184 retaining cap do not come off before the sample cylinder is placed inside the C80 [26].

185 The coal samples were collected in sample cylinders with uncontaminated interior walls

186 to reduce the experimental error of adsorption heat testing [34]. The whole test steps of

187 adsorption heat were shown as follows: (i) put coal into the sample cylinder and

188 tightened the cover with gasket; (ii) used special tweezers to install the snap-in spring,

189 followed by placing the sample cylinder inside the calorimetric unit; (iii) installed the

190 heat shielding assembly and waited for the HF signal to stabilize before starting the test.

191 During AFM scanning, the surface roughness and adhesion properties of different

192 coal samples were tested separately in the PeakForce QNM^{TM} mode. Before adjusting

193 the detector position, the laser should hit the front section of the cantilever, and the

194 same type of probe was selected for all coal samples [22]. It is worth noting that the

195 probe position should be found in the field of view in advance before starting the scan

196 to prevent the occurrence of needle collision [42].

197 **3. Methodology**

198 *3.1. Evaluation of adsorption potential*

199 During the adsorption process, methane is in the adsorption field on the coal surface,

200 so the adsorbent can be adsorbed onto the solid adsorbent surface [43, 44]. When the

201 effect of adsorption is greater than the molecular thermal motion, the distance between

202 the molecules of the adsorbent decreases, and even condensation or chemisorption

203 occurs [45, 46]. The concentration of the adsorbed phase, which is in the adsorption

204 layer between the adsorbent bulk phase and the solid adsorbent surface, generally varies

205 continuously in a gradient [18]. The existing theory of adsorption potential suggests

206 that the main force of gas-solid adsorption is the dispersion force, i.e., molecules can

207 be attracted to each other by temporary dipoles when they are close to each other [19,

208 27, 45]. Due to the constant movement of electrons and the vibration of the nucleus,

209 molecules often undergo temporary relative displacement between the electron cloud

210 and the nucleus, resulting in temporary dipoles. The dispersion force is mainly related

211 to molecular deformation, but not to temperature. Based on Polanyi's theory, the

212 adsorption potential ε is calculated as follows [47]:

213
$$\varepsilon = \mathrm{R}T\ln\frac{P_s}{P} \tag{1}$$

214 where R denotes the ideal gas constant; T represents the temperature; P_s indicates the

215 saturated vapor pressure at temperature T, and P is the equilibrium pressure.

216
$$P_s = P_c\left(\frac{T}{T_c}\right)^2 \tag{2}$$

217 where P_c denotes the constant critical pressure of methane; T_c stands for the constant

218 critical temperature of methane.

219
$$\varepsilon = \mathrm{R}T\ln\frac{P_c T^2}{P T_c^2} \tag{3}$$

220 *3.2. Pore characterization*

221   There are several pore classification schemes internationally, among which pores in

222 coal can be divided into adsorption pores (<100 nm) and seepage pores (100-1000 nm)

223 by combining various pore classification methods with the actual geology of Qinshui

224 Basin [11]. To accurately characterize the multiscale pores, FS-SEM and AFM were

225   combined to evaluate the differences in the spatial evolution of fluid flow in coal (Fig.

226   3). All coal samples must be polished prior to the scanning test to reduce the adhesion

227   of the pulverized coal particles [10]. In the scanning process of FS-SEM, the focus

228   swing function is first turned on to check whether the aperture is in alignment [20], and

229   then the astigmatism is checked by observing the astigmatism value in the status bar. In

230   general, the thermal field emission electron gun is a tungsten filament coated with

231   zirconia [48]. With the increase of using time, the zirconia crystal decreases, resulting

232   in the reduction of electron beam current. Therefore, the zirconia coating on the surface

233   of the electron gun filament should be ensured to meet the standard every time the coal

234   sample is tested.

235   AFM achieves detection by means of a micro-cantilever feeling the force between a

236   sharp probe and the atoms of samples [5, 22, 49]. In this study, the watershed method

237   was used to study the structure and developmental characteristics of pores in coal, so

238   that the threshold values of different ranges of pores could be determined without

239   artificial interference [22]. To obtain information on the curved undulations of the coal

240   surface, the change in position of the micro-cantilever corresponding to each point of

241   the scan was quantified by optical detection. Due to a large number of noise points in

242   the initially scanned images, the first-order Flatten method in NanoScope Analysis

243   software was used for noise reduction to acquire accurate pore parameters [42].

244   Subsequently, the roughness distribution characteristics of the coal surface were

245   evaluated by the 3D Image module. For fluid flow spatial connectivity, the Invert

246   Height function in Gwyddion software was used to determine the distribution of pores

247 at different scales in coal. In the process of AFM testing, the roughness can be

248 characterized by amplitude because the amplitude parameter can reflect the high and

249 low undulations of the coal surface. For the scanning anomalies caused by coal powder,

250 the Flatten function was used to smooth out the images. After that, the mean roughness

251 and root mean square roughness are obtained by the statistical quantity function, similar

252 to in our previous publication [30].
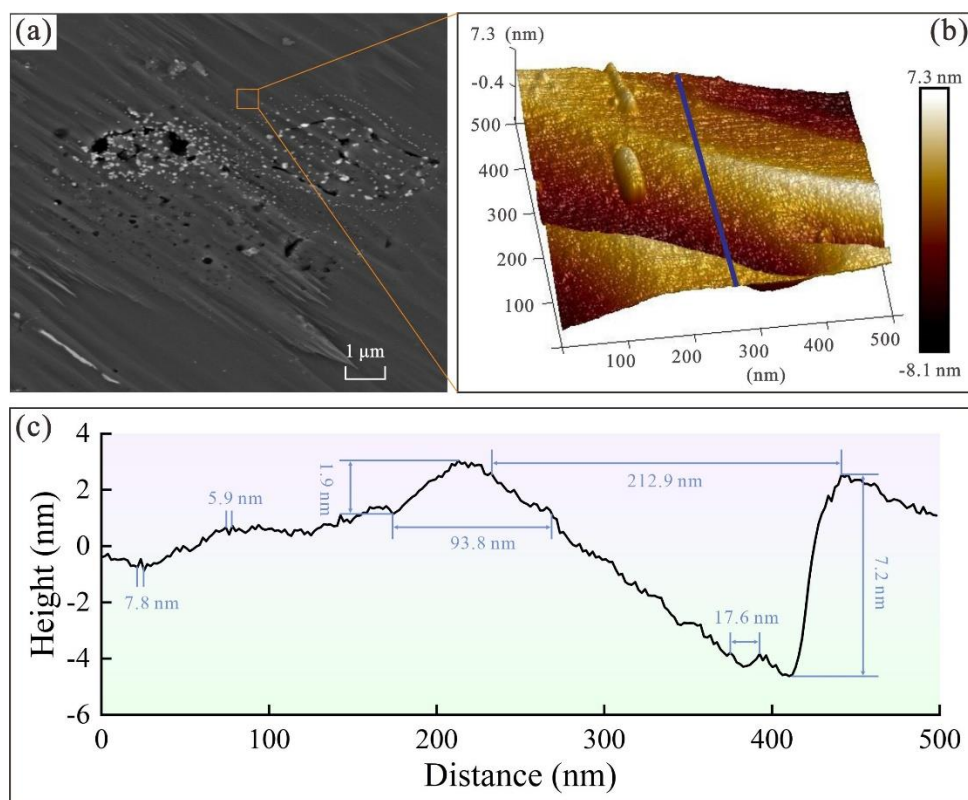
254 **Fig. 3.** Analysis of coal surface morphological characteristics by combining FS-SEM

255 and AFM. (a) FS-SEM measurement; (c) is the information of the bending undulation

256 of the blue straight line in the AFM scanning image (b).

3.3. Calculation of microscopic adhesion force

258   Methane molecules can be adsorbed to the surface of the coal matrix under the

259 action of adhesion force [18], which is the critical reason that CBM is mainly stored in

260 coal seam as adsorbed state [22]. In the PeakForce QNM^{TM} mode, AFM scans at a

261 frequency of 0.5 Hz, measuring more than 260,000 individual elements at a time. To

262 maintain a constant imaging effect, the peak force of each tap is used as a control signal

263 [5, 49]. Besides, each coal sample is calibrated before scanning to determine the

264 appropriate hardness of the probe.
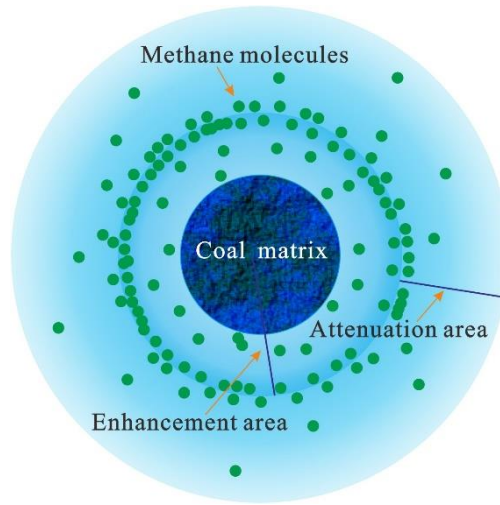
265

266 **Fig. 4.** Variation of adhesion force distribution on the surface of coal matrix.

267 As shown in Fig. 4, assuming the coal matrix as a spherical body, the adhesion force

268 on the surface tends to increase first and then decrease with increasing distance [8].

269 Methane molecules with low transport velocities can be easily adsorbed on the surface

270 of coal matrix, which provides some ideas for gas desorption. The calculation process

271 of adhesion force F_{adh} is as follows [22]:

272 $$F_{adh} = F_{tip} - \frac{4}{3} E^* \sqrt{rd^3} \qquad (4)$$

273 where F_{tip} shows the tip force; d represents the sample deformation; and r indicates the

274 tip radius. The equivalent modulus E^* is calculated as follows:

$$E^* = \left(\frac{1-v_s^2}{E_s} + \frac{1-v_{tip}^2}{E_{tip}} \right)^{-1} \qquad (5)$$

275

276 where E_s and E_{tip} denote the Young's modulus of coal sample and probe, respectively.

277 v_s and v_{tip} indicate the Poisson's ratio of coal sample and probe, respectively.

4. Results and discussion

278

4.1. Adsorption behavior in coals with different particle sizes

279

4.1.1. Adsorption properties of coals with different particle sizes

280

281 As a kind of porous media with strong heterogeneity, there are differences in

282 methane adsorption by coals with different particle sizes [3, 41]. The adsorption

283 saturation times of CZ for coal samples of 0.18-0.25, 0.43-0.85, 0.85-2.00 and 10-15

284 mm were about 72, 120, 168 and 500 h, respectively. The adsorption saturation times

285 of QY for coal samples with different particle sizes were about 70, 115, 157 and 483 h,

286 respectively. As shown in Fig. 5, the absolute adsorption volume (AAV) of coals with

287 different particle sizes tends to increase first and then stabilize as pressure increases,

288 with the maximum AAV reaching 36.03 cm^3/g. As the particle size increases, the

289 adsorption capacity of coal for methane gradually decreases. For the medium-rank coal

290 QY, the maximum AAV of 0.18-0.25 mm reaches 31.91 cm^3/g. The AAV of CZ of 0.85-

291 2.00 mm is 1.06 times higher than that of QY under the pressure condition of 4.2 MPa.

292 At different pressure conditions, the AAV of high-rank coal CZ (Fig. 5a) is greater than

293 that of medium-rank coal QY (Fig. 5b), which is similar to the results of Meng et al.

294 [19]. Moreover, with the increase in coal particle size, the adsorption capacity of CZ

15

295 changes more than QY, which is mainly related to the adsorption properties of coal [6].

296 In the adsorption process, the effective adsorption sites generally tend to decrease [24].

297 Due to the high density of free gas under low-pressure conditions, coal rocks exhibit a

298 strong ability to adsorb gas. The compressive strength of the coal rock increases with

299 increasing pressure causing some of the adsorption pores to deform or close, thereby

300 leading to the gradual saturation of adsorption capacity. Macroscopically, this variation

301 is shown by the decreasing trend of the adsorption rate with increasing pressure in Fig.

302 5.
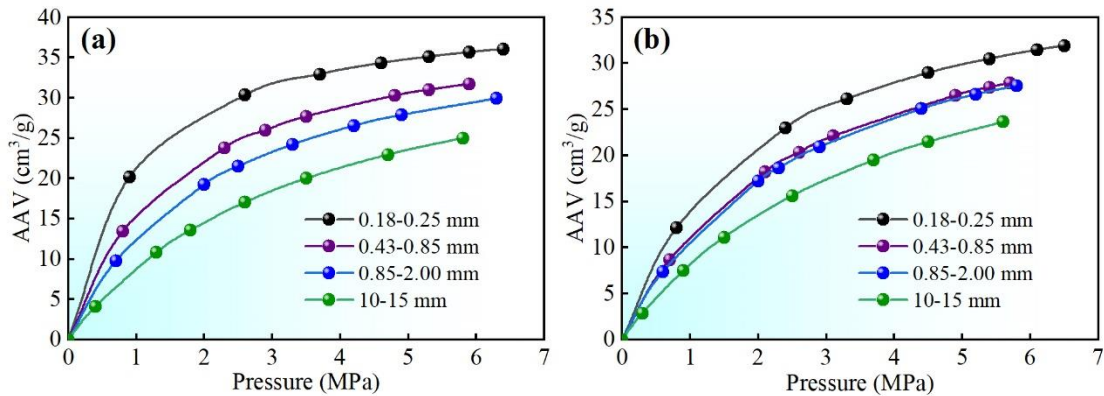
304 **Fig. 5.** The AAV of coal samples with different particle sizes at 25°C. (a) Coal sample

305 CZ; (b) Coal sample QY.

306 As reported by Du et al. [14]. the adsorption properties of coal are mainly controlled

307 by adsorption pore structure and surface chemical characteristics. Affected by the

308 degree of coalification, the micropores of high-rank coal are generally more developed

309 than that of medium-rank coal, resulting in a stronger adsorption capacity [50]. In the

310 process of magmatic thermal metamorphism, magma intrusion leads to aromatic group

311 rupture reducing the functional group content. Contrary to the adsorption of micropores,

312 this decreases the adsorption potential of high-rank coal for methane. However, the

313 negative effect of functional group reduction on the adsorption capacity is much smaller

314 than the positive effect of adsorption pores [6]. Therefore, the adsorption capacity of

315 CZ is stronger than QY.
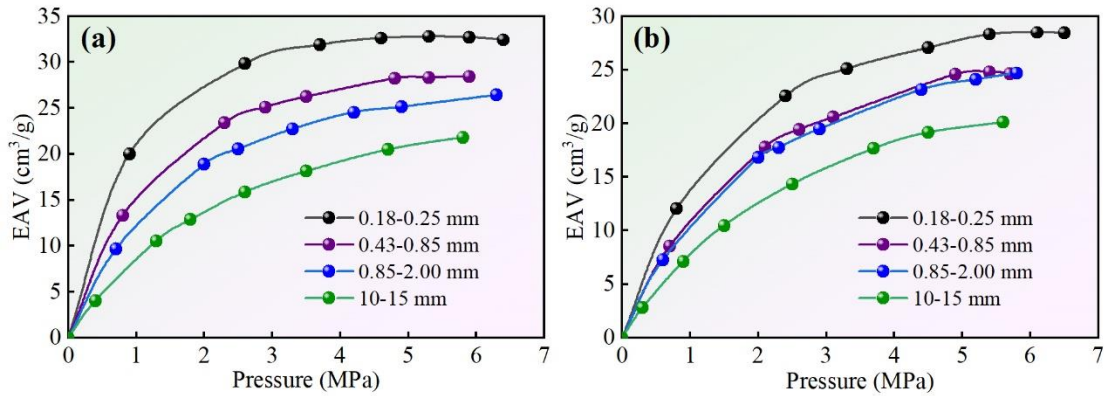
Fig. 6. The EAV of coal samples with different particle sizes at 25°C.

318 Similar to the AAV, the excess adsorption volume (EAV) of different coals shows

319 an overall trend of decreasing adsorption rate with increasing pressure (Fig. 6). When

320 the adsorption reaches equilibrium, the maximum EAV of CZ is 4 cm^3/g larger than that

321 of QY. At a pressure of 5.7 Ma, the EAV of CZ with 0.43-0.85 mm is 1.15 times larger

322 than that of QY. When the pressure is low, AAV is approximately equal to EAV (Figs.

323 5 and 6). With the increase of pressure, the difference between AAV and EAV increases,

324 indicating a gradual increase in the volume of adsorbed phase. Regardless of CZ or QY,

325 methane reaches the maximum adsorption volume when the residual adsorption

326 potential is 0. As the pressure continues to increase, more desorption occurs at different

327 sites of adsorbed phase [21], leading to the increase in the density of the free phase

328 methane increasing the gap between AAV and EAV. This is an essential characteristic

329 of supercritical methane, i.e., a downward trend in the EAV of supercritical methane in

330 coal occurs when the pressure is very high. Additionally, the more repulsive forces

331   between the gas molecules do work to generate more heat with the progress of

332   adsorption, which can also lead to desorption at different sites of the adsorbed phase.

333   *4.1.2. Temperature change during adsorption*

334   Due to the heat released during the adsorption process, the temperature of the coal

335   sample is in dynamic change [3, 51]. As presented in Fig. 7, there is a great difference

336   in the temperature variation of different particle size coal samples in the adsorption

337   process. With the increase of pressure, the temperature variation of coal during

338   adsorption decreases in a logarithmic pattern. The larger the particle size of coal, the

339   smaller the temperature variation. After reaching adsorption equilibrium, the

340   cumulative change in CZ for 0.18-0.25 mm ranges from 3.14°C (Fig. 7a). Whereas,

341   smaller changes occur in the CZ of 10-15 mm with a mere change of 1.78 °C. Similarly,

342   the QY of 0.43-0.85 mm varies by 0.63°C at the adsorption pressure of 0.7 MPa (Fig.

343   7b). However, the QY of 0.85-2.00 mm changes only 0.25°C at the adsorption pressure

344   of 5.8 MPa. In general, the temperature change of CZ during the adsorption reaching

345   equilibrium is greater than that of QY with the same particle size.
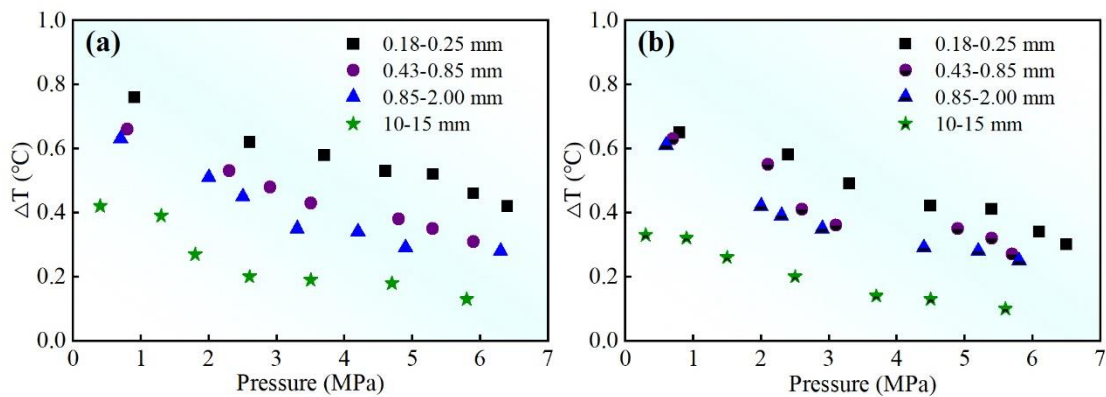
346

347   **Fig. 7.** Temperature variation of coal samples with different particle sizes during

348   adsorption.

349　　　In the adsorption process, the greater adsorption volume causes more heat to be

350　released, resulting in faster temperature changes [18]. On the contrary, the desorption

351　process of coal samples with different particle sizes undergoes changes in temperature

352　reduction [51]. Since the effect of temperature change affects the equilibrium of

353　adsorbed and free gas in coal, the diffusion and seepage linkage mechanism of coal in

354　the actual stratum changes accordingly. Also, this is an important reason for the change

355　in imbibition dynamics [52]. Therefore, the influence of temperature change should be

356　considered in the study of the elastic self-regulation effect of the CBM development

357　process.

358　*4.1.3. Constraint mechanism of temperature on adsorption*

359　　　As indicated in Fig. 8, temperature affects the adsorption capacity of coal samples

360　with different particle sizes. CZ exhibits similar isothermal adsorption curve

361　characteristics at different temperature conditions. When the CZ of 0.18-0.25 mm

362　reaches adsorption equilibrium, the AAV at 50°C is 8.68 cm^3/g less than that at 30°C.

363　For the CZ 10-15 mm, the AAV at 35°C is 1.11 times higher than that at 45°C. As can

364　be seen from Fig. 8, pressure is the main factor affecting CZ adsorption under low-

365　pressure conditions. With the increase of pressure, the temperature gradually becomes

366　the dominant factor controlling adsorption [34]. Also, QY with different particle sizes

367　displays similar curve characteristics, but the overall AAV at reaching adsorption

368　equilibrium is 1.37 to 4.12 cm^3/g smaller than CZ. These phenomena suggest that high

369　temperatures can provide the energy for gases to escape from coal surface, thus

370　reducing the adsorption affinity of coal [14]. In the actual CBM accumulation

development, the superimposed areas of syncline and anticline with larger burial depth contain small gas content [5, 15]. Hence, it is not recommended to drill CBM wells in these areas.

From Fig. 8, there are differences in the effect of temperature on the adsorption capacity of coal samples with different particle sizes. It is noteworthy that the difference in AAV at different temperatures gradually becomes smaller as the particle size of coal samples increases, mainly due to the relatively fewer adsorption sites for larger-size coal samples [2]. In other words, the influence of temperature on the adsorption sensitivity decreases with increasing coal sample size. In the process of CBM exploitation, the fragmented coal reservoir is generally more prone to CBM desorption than the primary structural coal reservoir. Since most of the underground coal seams have experienced multi-phase tectonic movement effects, fragmented coal is more susceptible to gas escape than fractured coal. Thus, the gas content of the same block of fragmented coal reservoir is generally lower than that of the fractured coal reservoir. For deep coal seams, temperature affects the permeability of the reservoir. On the one hand, the expansion of the coal-rock skeleton caused by heat leads to the narrowing of fluid channels reducing reservoir permeability. On the other hand, the increase in temperature decreases the viscosity of methane gas resulting in higher permeability of the reservoir. However, the influence of ground stress on CBM transport becomes increasingly significant as the depth of the coal seam increases, mainly reflecting the coupling effect of the paleo-tectonic stress field (controlling the generation of fractures in the coal) and the current stress field (controlling the opening degree of fractures).

393 Therefore, multiple factors (temperature, pressure, magma movement and tectonics,

394 etc.) should be considered for the development of deep-seated CBM.
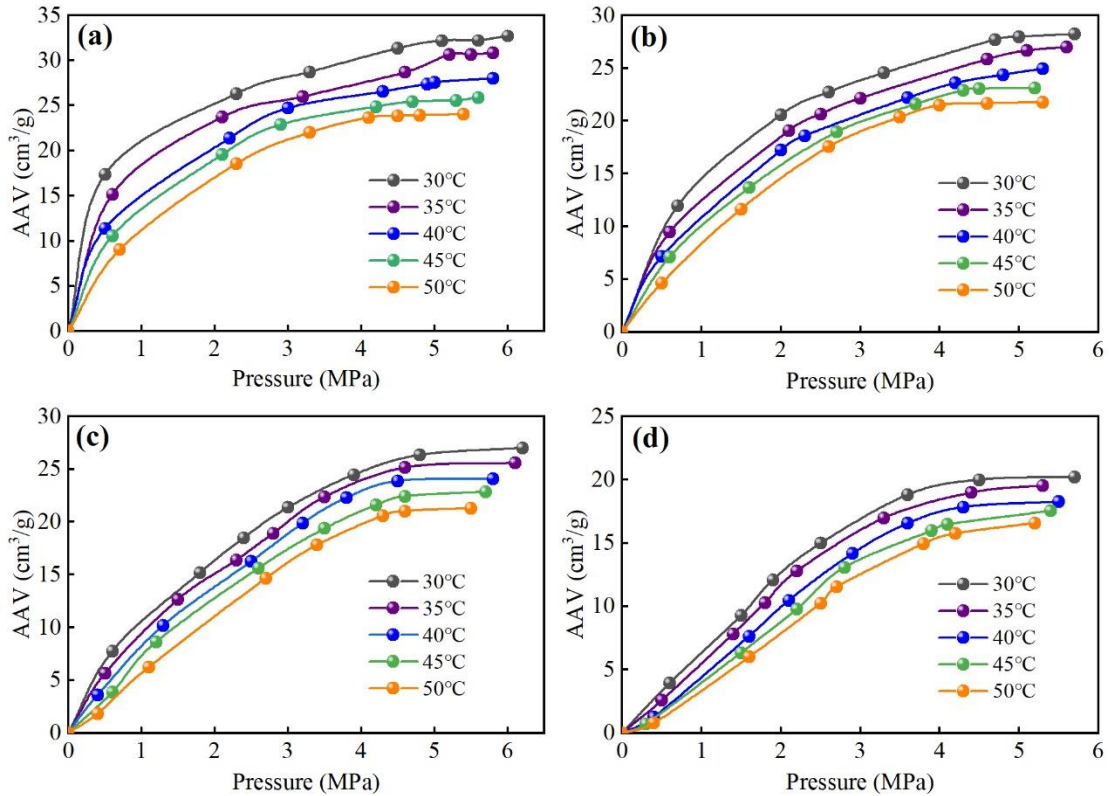
396 **Fig. 8.** Absolute adsorption volumes of CZ with different particle sizes at different

397 temperatures. (a) 0.18-0.25 mm; (b) 0.43-0.85 mm; (c) 0.85-2.00 mm; (d) 10-15 mm.

398 *4.1.4. Change in adsorption potential*

399   To further clarify the effect of temperature on adsorption, the adsorption potential

400 of coal samples at different temperatures was analyzed. As illustrated in Fig. 9, the

401 adsorption potential of the same particle size coal sample decreases with increasing

402 pressure. The higher the temperature, the greater the adsorption potential of coal. This

403 presents a new idea for improving CBM recovery [31]. The adsorption potential of CZ

404 reduces by 4.86 kJ/mol when saturation adsorption is reached at 25°C, while a greater

405 change in adsorption potential at 50°C can be found (decreased by 7 kJ/mol). In addition,

406   QY also exhibits a similar trend of adsorption potential variation. This indicates that the

407   increase in temperature decreases the energy required for the escape of gas molecules

408   from the coal surface, thus decreasing the adsorption potential [18]. Overall, the

409   adsorption potential of CZ is smaller than that of QY, which well confirms the variation

410   trends of AAV and EAV for both coal samples in Figs. 5 and 6.
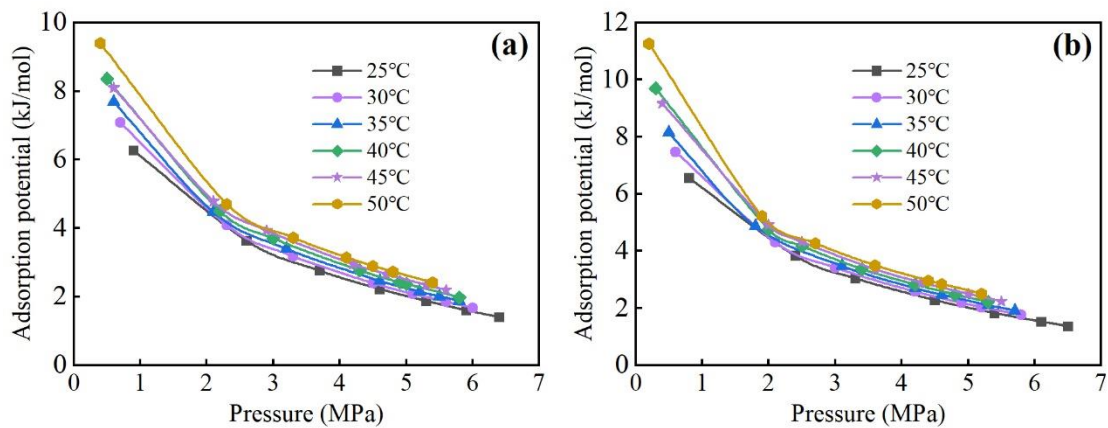
411

412   **Fig. 9.** Adsorption potential of coal samples of 0.18-0.25 mm at different temperatures.

413   (a) CZ; (b) QY.

414   The adsorption space and adsorption volume of low-particle size coal samples are

415   significantly higher than those of high-particle size coal samples, mainly due to the

416   combined effect of pore skeleton and macromolecular structure of coal during brittle

417   and ductile deformations [24]. In the process of multi-stage tectonic movement, the

418   adsorption space of coal increases with the enhancement of tectonic deformation, which

419   also provides more possibilities for methane to escape from coal seams to the roof and

420   floor [33].

421   *4.2. Impact of different scale pores in coal on adsorption effect*

422   Coal, as a porous medium with strong heterogeneity, contains pore-fractures of

different scales [3, 8, 53]. Due to the existence of primary, metamorphic, mineral and

epigenetic pores in coal, the adsorption process is complicated [6, 25, 54]. As indicated

in Fig. 10a$_1$ and b$_1$, there are differences in the pore distribution of CZ and QY. The

former contains many clustered pores, while the latter is mainly dominated by slit-like

pores. The CZ contains 2026 adsorption pores (Fig. 10a$_2$), with an average pore size of

3.06 nm. Interestingly, super-micropores smaller than 2 nm account for 67%. The

adsorption capacity of CZ is stronger because the super-micropores in coal contribute

to the major adsorption capacity. According to Fig. 10b$_2$, QY includes 1686 adsorption

pores, accounting for 8.56% of the coal sample area. An unexpected result is that the

average pore size of QY differs from that of CZ by 0.01 nm. However, the adsorption

pores from 2 to 100 nm account for 51%. Thus, the adsorption capacity of QY is weaker

than that of CZ. It is noteworthy that many closed pores are broken as the particle sizes

of coal samples decrease [21]. This is also an influential factor that the adsorption

capacity of the coal samples of 0.18-0.25 mm is stronger than that of 10-15 mm.

Due to the microscopic undulations of the planes that can represent the overall

concave and convex distribution of pores [5, 55], the roughness of coal was

characterized by AFM. The amplitude in the AFM image reflects the height change of

the coal surface, and the roughness analysis method has been mentioned in our previous

study [30]. As demonstrated in Fig. 11a, CZ exhibits the mean roughness of 2.09 nm

and the root mean square roughness of 1.46 nm. While, the lower roughness variation

is reflected in QY. the average roughness of QY is 1.48 nm smaller than that of CZ, and

the root mean square roughness is only one-third of CZ. These experimental results

445 suggest that the high complexity of surface fluctuations in CZ leads to a higher

446 resistance to transport of adsorbed methane. Besides, the adsorption pores on the

447 surface of CZ are more heterogeneous, which may result in more methane forming

448 capillary coalescence effects [2, 5].
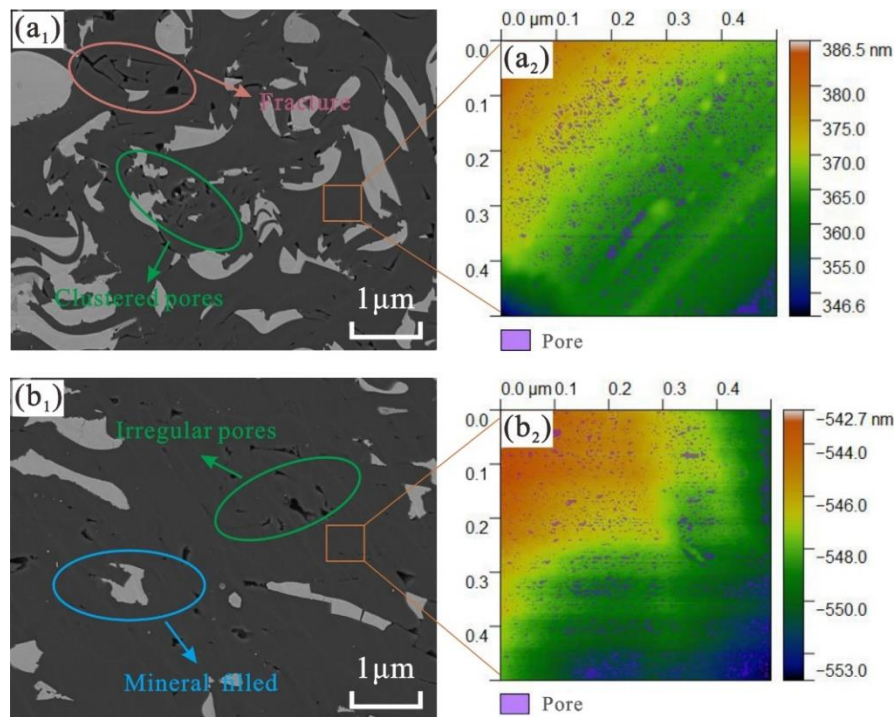
449

450 **Fig. 10.** Observation of microscopic pores in coal by FE-SEM and AFM.

451 *4.3. Evaluation of adsorption heat*

452 As illustrated in Fig. 12, The adsorption heat of coal samples with different particle

453 sizes shows a trend of "increasing first and then stabilizing" with increasing pressure.

454 As the particle size increases, the overall adsorption heat of coal tends to decrease. The

455 adsorption heat of CZ of 0.18-0.25 mm is higher than that of 0.85-2.00 mm by 3.57 J/g

456 for reaching the adsorption equilibrium at 25°C (Fig. 12a and c). However, greater

457 variation occurs in QY under the same conditions. When the coal sample reaches

458 adsorption equilibrium at 50°C, the adsorption heat of QY of 0.43-0.85 mm is about

459 1.08 times higher than that of 0.85-2.00 mm (Fig. 12e and f). This corroborates the

460 experimental results in Figs. 5 and 6, indicating that the larger the particle size of the

461 coal sample, the worse the adsorption capacity. Interestingly, the adsorption heat of CZ

462 is always greater than that of QY throughout the adsorption process. This may be related

463 to the structure of the coal itself [3, 30, 56], that is, high-rank coal is more strongly

464 metamorphosed by magma intrusion than medium-rank coal, forming more micropores

465 that are favorable for methane adsorption.
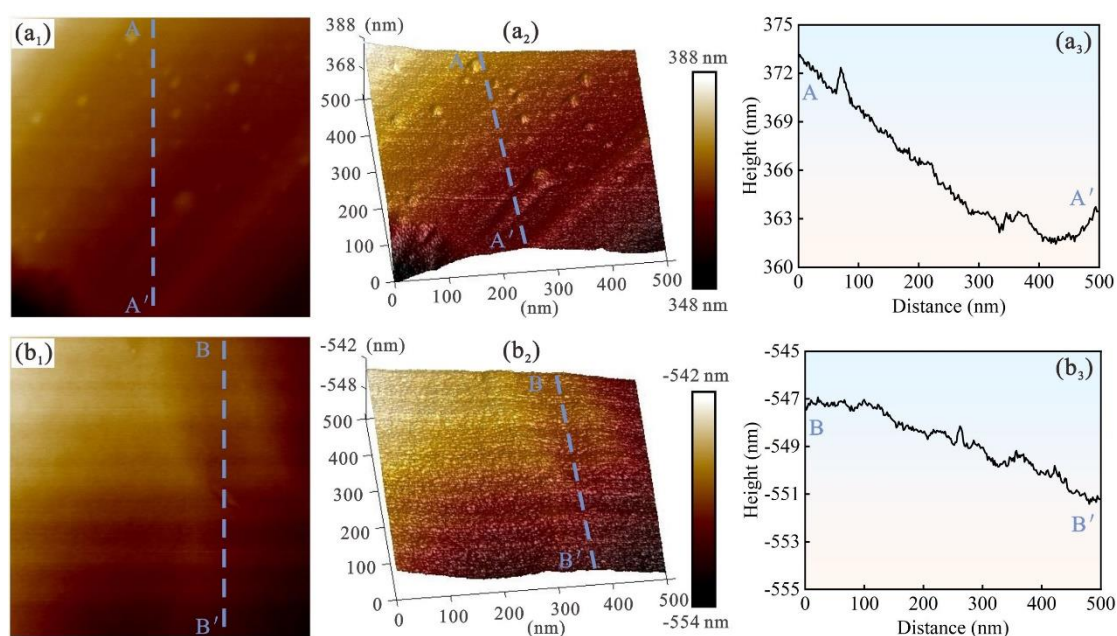
467 **Fig. 11.** AFM characterization of the concave and convex changes of coal surface in

468 two and three dimensions.

469　　As can be seen from Fig. 12, the adsorption heat of both coal samples is below 40

470 J/g, demonstrating that the physical adsorption of methane is mainly dominated by both

471 coal samples. Due to the strong heterogeneity of coal, methane tends to occupy sites

472 with high adsorption potential at the beginning of adsorption to release large amounts

473 of heat [50]. As the adsorption process proceeds, the later methane molecules can only

25

occupy adsorption sites with low adsorption potential to release a small amount of heat

[18]. Thus, the adsorption heat of coal samples with different particle sizes tends to

increase first and then stabilize with increasing pressure. In addition, the whole

adsorption is a process of van der Waals force interaction between methane molecules

and coal surface [1, 15]. Therefore, the intermolecular forces of adsorbed methane are

no longer negligible, which in turn causes the adsorption potential on the coal surface

to change, resulting in further enhancement of the heterogeneity of coal.
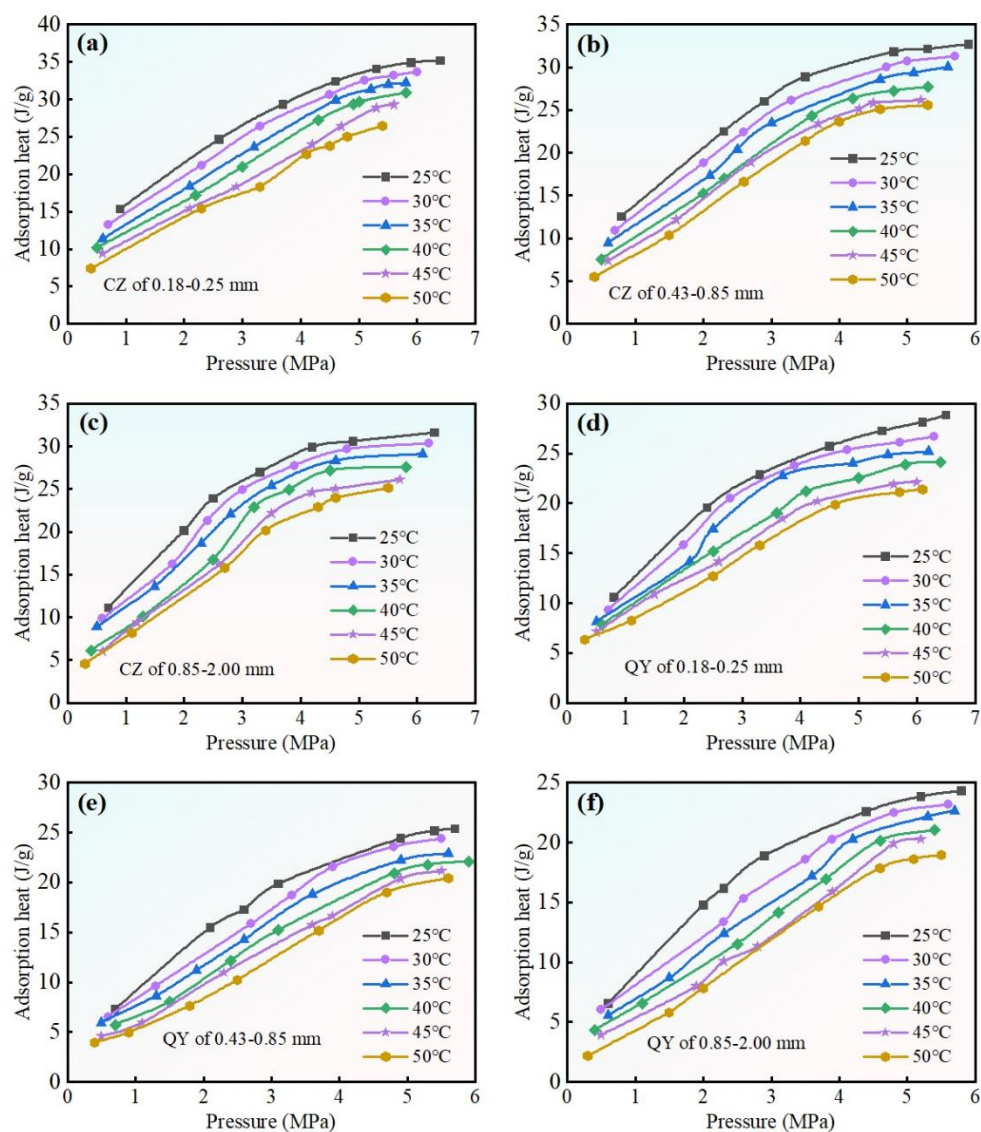
Fig. 12. Variation of adsorption heat of coal samples with different particle sizes at

different temperatures.
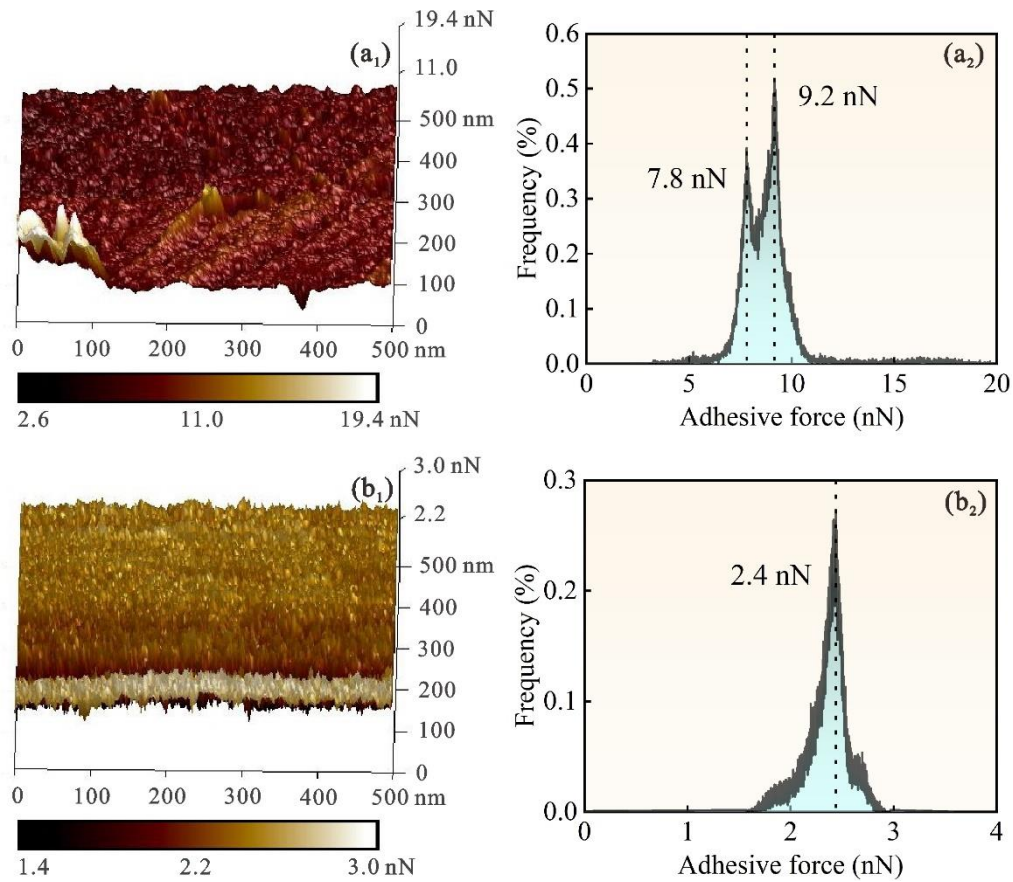
**Fig. 13.** The distribution of adhesion force of different coal samples at 25°C.

4.4. Microscopic adhesion variations in coal

To further reveal the adsorption mechanism of coal, the adhesion properties of different coal samples were characterized [30]. As indicated in Fig. 13, we counted the adhesion distribution of 2050 points in the 500 × 500 nm area of each coal sample. The adhesion force of CZ is distributed between 2.7 and 19.4 nN, with 9.2 nN accounting for the largest percentage of 0.5% (Fig. 13a_1 and a_2). The adhesion force is a comprehensive reflection of van der Waals, capillary and Coulomb forces [1, 8], indicating that the heterogeneity of the micromechanics in coal still exists. In contrast, the adhesion force distribution of QY is more uniform than that of CZ, mainly

27

concentrated between 1.5 and 3.0 nN (Fig. 13b$_1$ and b$_2$). In the process of methane

adsorption, gas molecules move on the surface of coal matrix. Affected by the adhesion

force, methane molecules in the effective adhesion region can be stably adsorbed into

pores [5, 57]. The adsorption process can be regarded as the comprehensive effect of

the adhesion between gas molecules and pores, making the adsorbed gas in dynamic

equilibrium with the free gas in coal [22]. Hence, this essentially clarifies that the

adsorption capacity of CZ is stronger than that of QY. The adhesion force is a critical

factor in determining the adsorption capacity of coal on methane [8], which provides a

new idea to expand the adsorption kinetics.

Temperature affects the microscopic adhesion, thereby changing the coal adsorption

properties of methane [24, 30]. From Fig. 14, the adhesion of coal tends to decrease

logarithmically with increasing temperature. This well explains the decrease in the

adsorption capacity of coal for methane with the increase of temperature. Moreover, the

higher the temperature, the more concentrated the adhesion distribution of coal,

indicating that temperature affects the heterogeneity of adhesion [6, 58]. It should be

noted that rising temperature increases the activation energy of the gas [8, 59], causing

the thermal motion of the methane molecules to accelerate. This reduces the adsorption

potential energy of methane molecules on the surface of coal matrix, resulting in an

enhanced rate of desorption of methane from coal. Since the desorption effect

essentially acts as an endothermic process, rising temperature disrupts the original

equilibrium state of adsorption-desorption, leading to the development of fluid

migration in the coal reservoir in a favorable direction [60, 61]. In particular, the

desorption efficiency of coals with different degrees of metamorphism is obviously

increased by rising temperature, further making the desorption hysteresis weaker.
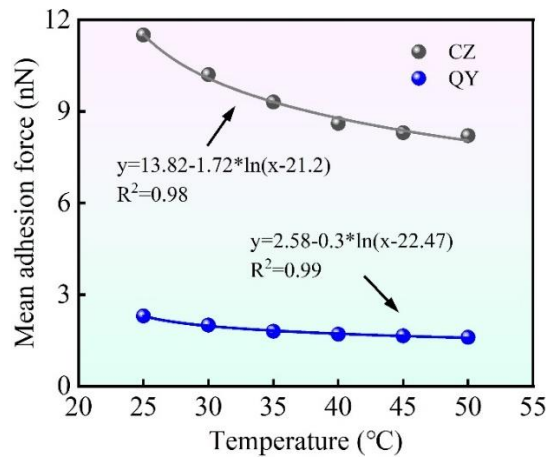
Fig. 14. Adhesion in coal at different temperatures.

5. Conclusions

In this work, we first investigated the adsorption properties of coals with different

particle sizes, followed by clarifying the effect of pores in coal at different scales on the

adsorption heat. To further elucidate the constraint mechanism of coal adsorption on

methane, the adsorption effects of coals with different particle sizes were dissected from

the perspective of microscopic adhesion considering the combined effects of van der

Waals, capillary and Coulomb forces. The following conclusions are drawn:

(1) As the pressure continues to increase, more desorption occurs at different sites of

adsorbed phase, leading to the increase in the density of the free phase methane

increasing the gap between AAV and EAV. This is an essential characteristic of

supercritical methane, i.e., a downward trend in the EAV of supercritical methane

in coal occurs when the pressure is very high.

(2) The CZ contains 2026 adsorption pores, with an average pore size of 3.06 nm.

Interestingly, super-micropores smaller than 2 nm account for 67%. The heterogeneity of the adsorption pores in CZ is stronger than in QY, resulting in the formation of more methane capillary condensation.

(3) The adsorption heat of CZ of 0.18-0.25 mm is higher than that of 0.85-2.00 mm by 3.57 J/g for reaching the adsorption equilibrium at 25°C. Due to the strong heterogeneity of coal, methane tends to occupy sites with high adsorption potential at the beginning of adsorption to release large amounts of heat.

(4) The adhesion force distribution of QY is more uniform than that of CZ, mainly concentrated between 1.5 and 3.0 nN. Affected by the adhesion force, methane molecules in the effective adhesion region can be stably adsorbed into pores. Moreover, the higher the temperature, the more concentrated the adhesion distribution of coal, indicating that temperature affects the heterogeneity of adhesion.

Declaration of Competing interests

The authors declare that they have no known competing financial interests or personal relationships that could have appeared to influence the work reported in this paper.

Acknowledgements

very grateful to the reviewers and editors for their valuable comments and suggestions.

Nomenclature

ε Adsorption potential [kJ/mol]

R   Ideal gas constant [kJ/(mol·K)]

T Temperature [K]

P_s Saturated vapor pressure at temperature T [MPa]

P Equilibrium pressure [MPa]

P_c Constant critical pressure of methane s [MPa]

T_c Constant critical temperature of methane [MPa]

F_{adh} Adhesion force [nN]

F_{tip} Tip force [nN]

E^* Reduced modulus [nm]

d Amount of sample deformation [nm]

r Tip radius [nm]

v_s The Poisson's ratio of coal sample

E_s The Young's modulus of coal sample [GPa]

v_{tip} The Poisson's ratio of probe

E_{tip} The Young's modulus of probe [GPa]

References

[1] J. Kang, D. Elsworth, X. Fu, S. Liang, H. Chen, Contribution of thermal expansion on gas adsorption to coal sorption-induced swelling, Chem. Eng. J. 432 (2022) 134427, https://doi.org/10.1016/j.cej.2021.134427.

[2] Y. Li, Z. Wang, S. Tang, D. Elsworth, Re-evaluating adsorbed and free methane content in coal and its ad- and desorption processes analysis, Chem. Eng. J. 428 (2022) 131946, https://doi.org/10.1016/j.cej.2021.131946.

[3] D. Liu, Y. Yao, Y. Chang, Measurement of adsorption phase densities with respect to different pressure: Potential application for determination of free and adsorbed methane in coalbed methane reservoir, Chem. Eng. J. 446 (2022) 137103, https://doi.org/10.1016/j.cej.2022.137103.

[4] D. Liu, Y. Yao, X. Yuan, Y. Yang, Experimental evaluation of the dynamic water-blocking effect in coalbed methane reservoir, J. Petrol. Sci. Eng. 217 (2022) 110887, https://doi.org/10.1016/j.petrol.2022.110887.

[5] Y. Li, J. Yang, Z. Pan, W. Tong, Nanoscale pore structure and mechanical property analysis of coal: An insight combining AFM and SEM images, Fuel 260 (2020) 116352, https://doi.org/10.1016/j.fuel.2019.116352.

[6] Y. Xu, Z. Lun, Z. Pan, H. Wang, X. Zhou, C. Zhao, D. Zhang, Occurrence space and state of shale oil: A review, J. Petrol. Sci. Eng. 211 (2022) 110183, https://doi.org/10.1016/j.petrol.2022.110183.

[7] J. Deng, J. Kang, F. Zhou, H. Li, D. Zhang, G. Li, The adsorption heat of methane on coal: Comparison of theoretical and calorimetric heat and model of heat flow by microcalorimeter, Fuel 237 (2019) 81-90. https://doi.org/10.1016/j.fuel.2018.09.123.

[8] X. Tian, D. Song, X. He, Z. Li, H. Liu, W. Wang, Investigation on micro-surface adhesion of coals and implications for gas occurrence and coal and gas outburst mechanism, J. Nat. Gas Sci. Eng. 94 (2021) 104115, https://doi.org/10.1016/j.jngse.2021.104115.

[9] Q. Jia, D. Liu, Y. Cai, X. Fang, L. Li, Petrophysics characteristics of coalbed methane reservoir: A comprehensive review, Front. Earth Sci. 15(2) (2020) 202-223. https://doi.org/10.1007/s11707-020-0833-1.

[10] Z. Liu, D. Liu, Y. Cai, Y. Qiu, Permeability, mineral and pore characteristics of coals response to acid treatment by NMR and QEMSCAN: Insights into acid sensitivity mechanism, J. Petrol. Sci. Eng. 198 (2021) 108205, https://doi.org/10.1016/j.petrol.2020.108205.

[11] Y. Cai, D. Liu, Z. Pan, Y. Yao, J. Li, Y. Qiu, Pore structure and its impact on CH4 adsorption capacity and flow capability of bituminous and subbituminous coals from Northeast China, Fuel 103 (2013) 258-268. https://doi.org/10.1016/j.fuel.2012.06.055.

[12] Q. Li, D. Liu, Y. Cai, B. Zhao, Y. Lu, Y. Zhou, Effects of natural micro-fracture morphology, temperature and pressure on fluid flow in coals through fractal theory combined with lattice Boltzmann method, Fuel 286 (2021) 119468, https://doi.org/10.1016/j.fuel.2020.119468.

[13] J. Kang, R. Wan, F. Zhou, Y. Liu, Z. Li, Y. Yin, Effects of supercritical CO_2 extraction on adsorption characteristics of methane on different types of coals, Chem. Eng. J. 388 (2020) 123449, https://doi.org/10.1016/j.cej.2019.123449.

[14] X. Du, Y. Cheng, Z. Liu, H. Yin, T. Wu, L. Huo, C. Shu, CO_2 and CH4 adsorption on different rank coals: A thermodynamics study of surface potential, Gibbs free energy change and entropy loss, Fuel 283 (2021) 118886, https://doi.org/10.1016/j.fuel.2020.118886.

[15] Q. Jia, D. Liu, X. Ni, Y. Cai, Y. Lu, Z. Li, Y. Zhou, Interference mechanism in coalbed methane wells and impacts on infill adjustment for existing well patterns, Energy Rep. 8 (2022) 8675-8689. https://doi.org/10.1016/j.egyr.2022.06.070.

[16] X. Zhang, B. Lin, J. Shen, Experimental research on the effect of plasma on the pore-fracture

structures and adsorption-desorption of coal body, Fuel 307 (2022) 121809, https://doi.org/10.1016/j.fuel.2021.121809.

[17] X. Zhang, B. Lin, J. Shen, Study on the improvement of permeability of loaded bituminous coal after plasma breakdown, Fuel 310 (2022) 122431, https://doi.org/10.1016/j.fuel.2021.122431.

[18] D. Liu, Z. Zou, Y. Cai, Y. Qiu, Y. Zhou, S. He, An updated study on CH_4 isothermal adsorption and isosteric adsorption heat behaviors of variable rank coals, J. Nat. Gas Sci. Eng. 89 (2021) 103899, https://doi.org/10.1016/j.jngse.2021.103899.

[19] Z. Meng, S. Liu, G. Li, Adsorption capacity, adsorption potential and surface free energy of different structure high rank coals, J. Petrol. Sci. Eng. 146 (2016) 856-865. https://doi.org/10.1016/j.petrol.2016.07.026.

[20] Q. Gou, S. Xu, F. Hao, F. Yang, B. Zhang, Z. Shu, A. Zhang, Y. Wang, Y. Lu, X. Cheng, J. Qing, M. Gao, Full-scale pores and micro-fractures characterization using FE-SEM, gas adsorption, nano-CT and micro-CT: A case study of the Silurian Longmaxi Formation shale in the Fuling area, Sichuan Basin, China, Fuel 253 (2019) 167-179. https://doi.org/10.1016/j.fuel.2019.04.116.

[21] Y. Chen, D. Ma, C. Guo, F. Yang, T. Mu, Z. Gao, An Experimental Study on the Conductivity Changes in Coal during Methane Adsorption-Desorption and their Influencing Factors, Acta Geol. Sin. - Engl. 93(3) (2019) 704-717. https://doi.org/10.1111/1755-6724.13873.

[22] Y. Lu, D. Liu, Y. Cai, C. Gao, Q. Jia, Y. Zhou, AFM measurement of roughness, adhesive force and wettability in various rank coal samples from Qinshui and Junggar basin, China, Fuel 317 (2022) 123556, https://doi.org/10.1016/j.fuel.2022.123556.

644 [23] K. Zhang, Z. Meng, S. Liu, Comparisons of Methane Adsorption/Desorption, Diffusion

645 Behaviors on Intact Coals and Deformed Coals: Based on Experimental Analysis and Isosteric

646 Heat of Adsorption, Energ. Fuel. 35(7) (2021) 5975-5987.

647 https://doi.org/10.1021/acs.energyfuels.1c00325.

648 [24] X. Fu, C. Zhao, Z. Lun, H. Wang, M. Wang, D. Zhang, Influences of controlled microwave

649 field radiation on pore structure, surface chemistry and adsorption capability of gas-bearing

650 shales, Mar. Petrol. Geol. 130 (2021) 105134,

651 https://doi.org/10.1016/j.marpetgeo.2021.105134.

652 [25] D. Zhang, C. Li, J. Zhang, Z. Lun, S. Jia, C. Luo, W. Jiang, Influences of dynamic entrainer-

653 blended supercritical CO_2 fluid exposure on high-pressure methane adsorption on coals, J. Nat.

654 Gas Sci. Eng. 66 (2019) 180-191. https://doi.org/10.1016/j.jngse.2019.03.031.

655 [26] X. Zhang, S. Zhang, Z. Du, G.G.X. Wang, S. Heng, X. Liu, J. Lin, CO_2 and N_2

656 adsorption/desorption effects and thermodynamic characteristics in confined coal, J. Petrol. Sci.

657 Eng. 207 (2021) 109166, https://doi.org/10.1016/j.petrol.2021.109166.

658 [27] T. Gao, D. Zhao, C. Wang, Z. Feng, Energy variation in coal samples with different particle

659 sizes in the process of adsorption and desorption, J. Petrol. Sci. Eng. 188 (2020) 106932,

660 https://doi.org/10.1016/j.petrol.2020.106932.

661 [28] S. Wang, Y. Hu, X. Yang, G. Liu, Y. He, Examination of adsorption behaviors of carbon dioxide

662 and methane in oxidized coal seams, Fuel 273 (2020) 117599,

663 https://doi.org/10.1016/j.fuel.2020.117599.

664 [29] J. Xiang, F. Zeng, H. Liang, B. Li, X. Song, Molecular simulation of the CH4/CO2/H2O

665 adsorption onto the molecular structure of coal, Sci. China Earth Sci. 57(8) (2014) 1749-1759.

https://doi.org/10.1007/s11430-014-4849-9.

[30] Q. Jia, D. Liu, Y. Cai, Y. Zhou, Z. Zhao, Y. Yang, AFM characterization of physical properties in coal adsorbed with different cations induced by electric pulse fracturing, Fuel 327 (2022) 125247, https://doi.org/10.1016/j.fuel.2022.125247.

[31] J. Kang, X. Fu, X. Li, S. Liang, Nitrogen injection to enhance methane and water production: An experimental study using the LF-NMR relaxation method, Int. J. Coal Geol. 211 (2019) 103228, https://doi.org/10.1016/j.coal.2019.103228.

[32] F. Zhou, S. Liu, Y. Pang, J. Li, H. Xin, Effects of Coal Functional Groups on Adsorption Microheat of Coal Bed Methane, Energ. Fuel. 29(3) (2015) 1550-1557. https://doi.org/10.1021/ef502718s.

[33] D. Liu, Y. Yao, H. Wang, Structural compartmentalization and its relationships with gas accumulation and gas production in the Zhengzhuang Field, southern Qinshui Basin, Int. J. Coal Geol. 259 (2022) 104055, https://doi.org/10.1016/j.coal.2022.104055.

[34] M. Hao, Z. Qiao, H. Zhang, Y. Wang, Y. Li, Thermodynamic Analysis of CH4/CO2/N2 Adsorption on Anthracite Coal: Investigated by Molecular Simulation, Energ. Fuel. 35(5) (2021) 4246-4257. https://doi.org/10.1021/acs.energyfuels.0c04337.

[35] Y. Li, H. Cui, P. Zhang, D. Wang, J. Wei, Three-dimensional visualization and quantitative characterization of coal fracture dynamic evolution under uniaxial and triaxial compression based on μCT scanning, Fuel 262 (2020) 116568, https://doi.org/10.1016/j.fuel.2019.116568.

[36] A. Liu, P. Liu, S. Liu, Gas diffusion coefficient estimation of coal: A dimensionless numerical method and its experimental validation, Int. J. Heat Mass Tran. 162 (2020) 120336, https://doi.org/10.1016/j.ijheatmasstransfer.2020.120336.

[37] Z. Li, D. Liu, P.G. Ranjith, Y. Cai, Y. Wang, Geological controls on variable gas concentrations: A case study of the northern Gujiao Block, northwestern Qinshui Basin, China, Mar. Petrol. Geol. 92 (2018) 582-596. https://doi.org/10.1016/j.marpetgeo.2017.11.022.

[38] J. Ribeiro, I. Suárez-Ruiz, C.R. Ward, D. Flores, Petrography and mineralogy of self-burning coal wastes from anthracite mining in the El Bierzo Coalfield (NW Spain), Int. J. Coal Geol. 154-155 (2016) 92-106. https://doi.org/10.1016/j.coal.2015.12.011.

[39] Y.I. Aristov, Adsorption heat conversion and storage in closed systems: What have we learned over the past decade of this century?, Energy 239 (2022) 122142, https://doi.org/10.1016/j.energy.2021.122142.

[40] H.f. Lin, H. Long, M. Yan, S.-g. Li, C.M. Shu, Y. Bai, Methane adsorption thermodynamics of coal sample subjected to liquid nitrogen freezing–thawing process, J. Nat. Gas Sci. Eng. 90 (2021) 103896, https://doi.org/10.1016/j.jngse.2021.103896.

[41] S. Zhang, Z. Wang, X. Zhang, F. Chen, X. Ping, Z. Sun, Experimental study on physicochemical structure of different rank coals under acid solvent treatments and its effects on heat of gas adsorption, J. Petrol. Sci. Eng. 211 (2022) 110191, https://doi.org/10.1016/j.petrol.2022.110191.

[42] M. Eliyahu, S. Emmanuel, R.J. Day-Stirrat, C.I. Macaulay, Mechanical properties of organic matter in shales mapped at the nanometer scale, Mar. Petrol. Geol. 59 (2015) 294-304. https://doi.org/10.1016/j.marpetgeo.2014.09.007.

[43] M. Meng, Z. Qiu, R. Zhong, Z. Liu, Y. Liu, P. Chen, Adsorption characteristics of supercritical CO_2/CH_4 on different types of coal and a machine learning approach, Chem. Eng. J. 368 (2019) 847-864. https://doi.org/10.1016/j.cej.2019.03.008.

710 [44] W. Zhao, K. Wang, S. Liu, Y. Ju, H. Zhou, L. Fan, Y. Yang, Y. Cheng, X. Zhang, Asynchronous

711 difference in dynamic characteristics of adsorption swelling and mechanical compression of

712 coal: Modeling and experiments, Int. J. Rock Mech. Min. 135 (2020) 104498,

713 https://doi.org/10.1016/j.ijrmms.2020.104498.

714 [45] W. Zhou, K. Gao, S. Xue, Y. Han, C.-M. Shu, P. Huang, Experimental study of the effects of

715 gas adsorption on the mechanical properties of coal, Fuel 281 (2020) 118745,

716 https://doi.org/10.1016/j.fuel.2020.118745.

717 [46] Z. Wang, W. Su, X. Tang, J. Wu, Influence of water invasion on methane adsorption behavior

718 in coal, Int. J. Coal Geol. 197 (2018) 74-83. https://doi.org/10.1016/j.coal.2018.08.004.

719 [47] C.j. Zhu, J. Ren, J. Wan, B.-q. Lin, K. Yang, Y. Li, Methane adsorption on coals with different

720 coal rank under elevated temperature and pressure, Fuel 254 (2019) 115686,

721 https://doi.org/10.1016/j.fuel.2019.115686.

722 [48] J. Zhang, Y. Tang, D. He, P. Sun, X. Zou, Full-scale nanopore system and fractal characteristics

723 of clay-rich lacustrine shale combining FE-SEM, nano-CT, gas adsorption and mercury

724 intrusion porosimetry, Appl. Clay Sci. 196 (2020) 105758,

725 https://doi.org/10.1016/j.clay.2020.105758.

726 [49] S. Chen, X. Li, S. Chen, Y. Wang, Z. Gong, Y. Zhang, A new application of atomic force

727 microscopy in the characterization of pore structure and pore contribution in shale gas

728 reservoirs, J. Nat. Gas Sci. Eng. 88 (2021) 103802,

729 https://doi.org/10.1016/j.jngse.2021.103802.

730 [50] X. Fu, Z. Lun, C. Zhao, X. Zhou, H. Wang, X. Zhou, Y. Xu, H. Zhang, D. Zhang, Influences of

731 controlled microwave field irradiation on physicochemical property and methane adsorption

and desorption capability of coals: Implications for coalbed methane (CBM) production, Fuel

301 (2021) 121022, https://doi.org/10.1016/j.fuel.2021.121022.

[51] J. Hao, B. Liang, W. Sun, Experimental Study on the Thermal Effect during Gas Adsorption

and Desorption on the Coal Surface, ACS Omega 6(2) (2021) 1603-1611.

https://doi.org/10.1021/acsomega.0c05505.

[52] Y. Lu, D. Liu, Y. Cai, Q. Li, Y. Zhou, Spontaneous imbibition in coal with in-situ dynamic

micro-CT imaging, J. Petrol. Sci. Eng. 208 (2022) 109296,

https://doi.org/10.1016/j.petrol.2021.109296.

[53] D. Song, X. Liu, X. He, B. Nie, W. Wang, Investigation on the surface electrical characteristics

of coal and influencing factors, Fuel 287 (2021) 119551,

https://doi.org/10.1016/j.fuel.2020.119551.

[54] Y. Yao, D. Liu, Y. Che, D. Tang, S. Tang, W. Huang, Petrophysical characterization of coals by

low-field nuclear magnetic resonance (NMR), Fuel 89(7) (2010) 1371-1380.

https://doi.org/10.1016/j.fuel.2009.11.005.

[55] Y. Li, J. Chen, D. Elsworth, Z. Pan, X. Ma, Nanoscale mechanical property variations

concerning mineral composition and contact of marine shale, Geosci. Front. 13(4) (2022)

101405, https://doi.org/10.1016/j.gsf.2022.101405.

[56] H. Wang, Y. Yao, D. Liu, Y. Cai, Y. Yang, S. Zhou, Determination of the degree of coal

deformation and its effects on gas production in the southern Qinshui Basin, North China, J.

Petrol. Sci. Eng. 216 (2022) 110746, https://doi.org/10.1016/j.petrol.2022.110746.

[57] X. Lei, Y. Yao, X. Sun, Z. Wen, Y. Ma, Permeability change with respect to different hydrate

saturation in clayey-silty sediments, Energy 254 (2022) 124417,

754 https://doi.org/10.1016/j.energy.2022.124417.

755 [58] A. Roslin, D. Pokrajac, K. Wu, Y. Zhou, 3D pore system reconstruction using nano-scale 2D

756 SEM images and pore size distribution analysis for intermediate rank coal matrix, Fuel 275

757 (2020) 117934, https://doi.org/10.1016/j.fuel.2020.117934.

758 [59] Y. Zhou, J.O. Helland, E. Jettestuen, Dynamic capillary pressure curves from pore-scale

759 modeling in mixed-wet-rock images, SPE J. 18 (2013) 634-645,

760 https://doi.org/10.2118/154474-PA.

761 [60] C. Wang, K. Wu, G.G. Scott, A.R. Akisanya, Q. Gan, Y. Zhou, A new method for pore structure

762 quantification and pore network extraction from SEM images, Energ. Fuel. 34(1) (2019) 82-

763 94. https://doi.org/10.1021/acs.energyfuels.9b02522.

764 [61] Y. Zhou, J.O. Helland, D.G. Hatzignatiou, Computation of three-phase capillary pressure

765 curves and fluid configurations at mixed-wet conditions in 2D rock images, SPE J. 21 (2016)

766 152-169, https://doi.org/10.2118/170883-PA.